ELSEVIER

Eur. J. Mech. B/Fluids 21 (2002) 75–90

EUROPEAN JOURNAL OF MECHANICS B/FLUIDS

Natural convection in a liquid metal heated from above and influenced by a magnetic field

Christian Karcher *, Y. Kolesnikov, O. Andreev, A. Thess

Department of Mechanical Engineering, Ilmenau University of Technology, 98684 Ilmenau, Germany

Received 1 September 1999; received in revised form 6 February 2001; accepted 17 August 2001

Abstract

Natural convection in a liquid metal heated locally at its upper surface and affected by a vertical magnetic field is investigated both experimentally and numerically. The experiments are conducted in a cylindrical test cell of large aspect ratio which is typical for application. The cell is filled with the liquid alloy GaInSn in eutectic composition. Temperature and velocity are measured using thermocouples and an electric potential probe, respectively. In the absence of the magnetic field the experimental results indicate a dependence of the Nusselt number on the Rayleigh number according to the law $Nu \propto Ra^{0.191}$. The particular value of the scaling exponent is in excellent agreement with the prediction of a scaling analysis for laminar, boundary layer-type flow in a low-Prandtl number fluid. Furthermore the experiments demonstrate that the Nusselt number and therefore the convective heat losses can be decreased by about 20% when a magnetic field of moderate strength ($B = 0.1$ T) is present. The numerical simulations solve the Boussinesq equations in an axisymmetric geometry using a finite element method. The results of the simulations are both quantitatively and qualitatively in good agreement with the experimental observations. Deviations are attributed to the three-dimensional characteristics of the flow.

Keywords: Liquid metal flow; Magnetohydrodynamics; Convective heat transfer

1. Introduction

We study the effects of an externally applied vertical magnetic field on convective heat transfer in a liquid metal locally heated at its upper surface. The studies include velocity and temperature measurements in a cylindrical test cell as well as numerical simulations using a finite element method.

Motivation for the present investigations comes from electron beam evaporation of liquid metals (Schiller et al. [1]). In this innovative coating technology the surface of a melt, confined in a water-cooled crucible, is stimulated to evaporate by bombardment with a high-energy electron beam gun. The rising vapor cloud condenses as a thin film on a moving substrate located at some distance above. The strong energy flux from the electron beam induces strong temperature gradients along the surface and in the interior of the melt. Thus, the liquid metal is subject to vigorous motion due to both surface-tension-driven (cf. Davis [2]) and buoyancy-driven (cf. Siggia [3]) convection. The strong convective heat transfer limits the temperature rise at the surface and therefore the thermodynamic efficiency of the evaporation process. The basic scaling laws of convective heat transfer in a liquid heated on its free surface has been derived by Pumir and Blumenfeld [4] for both laminar and turbulent flow. Experimental investigations on convective flow and heat transfer include measurements in silicon oil (Favre et al. [5]) and in liquid iron under evaporation conditions (Karcher et al. [6]). There are two principle methods to reduce these highly unwelcome convective heat losses: (i) optimization of the geometry of the crucible (see Karcher et al. [7]); (ii) control of convection using

* Correspondence and reprints.
E-mail address: christian.karcher@mb.tu-ilmenau.de (C. Karcher).

0997-7546/02/$ – see front matter
PII: S0997-7546(01)01164-5

an applied magnetic field. Here one exploits the physical mechanism that in electrically conducting fluids, interactions between the applied magnetic field and fluid-flow generate a so-called Lorentz force within the melt, see, e.g., Moreau [8]. This body force may serve to slow down convective motion. The dampening effect of magnetic fields on surface-tension-driven convection typical for electron beam technologies was recently discussed by Marty [9] and Karcher [10]. In the present study we focus on the effect of a uniform vertical magnetic field on purely buoyancy-driven convection. In our laboratory experiment the surface of the melt (GaInSn) was covered by a thin oxide layer which excludes thermocapillary effects.

The application of magnetic fields in material processing and flow control shows a great variety, see Davidson [11] for a detailed review. Uniform magnetic fields can be used to suppress convective instabilities (see, e.g., Chandrasekhar [12], Boyarevich and Gorbunov [13], and Fauve et al. [14]), to suppress turbulence (see, e.g., Moffat [15]), and to dampen jets and vortices (see, e.g., Davidson [16]). Magnetic fields also represent a powerful tool to control free surface flows and interfacial instabilities, see, e.g., Rivat et al. [17], and Davidson and Lindsay [18]. Moreover, magnetic fields are commonly used in crystal growth applications, see Series and Hurle [19] for a detailed review. In these processes, to obtain high-quality semiconductor crystals it is crucial to suppress convective motion induced by the strong imposed horizontal heat flux. Experimental and theoretical work in this field include Papaliliou and Lykoudis [20], Seki et al. [21], Hjellming and Walker [22], and Okado and Ozoe [23], and more recently Tagawa and Ozoe [24] and Juel et al. [25]. The suppression of convective motion and heat transfer in a liquid metal heated from below was recently studied numerically by Li et al. [26]. However, in Li et al. [26] and Tagawa and Ozoe [24] it was found that weak magnetic fields may even act in opposite direction as they tend to enhance the convective heat transfer.

The present study investigates the effect of a vertical magnetic field on convective heat transfer in a liquid metal locally heated from above. The paper is organized as follows. In Section 2 we present the experimental set-up and show our measurement techniques. The methods used in the numerical simulations are described in Section 3. In Section 4 we present both our experimental and numerical results on convective heat transfer in a liquid metal affected by a static vertical magnetic field. Finally, in Section 5 we summarize our main findings.

2. Experimental set-up and measurement techniques

2.1. Description of the set-up

The experiments are carried out in a cylindrical container made of copper with an inside diameter of $2R = 165$ mm and a height of $H = 20$ mm. This yields an aspect ratio of $R/H = 4.125$. A sketch of the experimental device is shown in Fig. 1. The container is placed on an adjustable table to align the axis with the direction of gravity. The bottom and lateral wall of the container are kept at a constant temperature of $20 \pm 0.5\,^{\circ}\mathrm{C}$ by through flow of water fed from a refrigerated bath. Here the thickness of the inner copper walls is 5 mm. As working liquid we use the eutectic alloy GaInSn which has a melting temperature of $10.5\,^{\circ}\mathrm{C}$. The material properties of InGaSn are listed in Table 1. To ensure a good heat contact between the liquid metal and the container, we carefully clean the copper walls with HCl before filling. To reduce heat losses through the liquid surface during the experiments, the container is covered by the 8 mm thick thermoinsulating plate with a narrow slot of 4 mm for probe movement. To minimize air convection above the hot fluid, the gap between the liquid surface and the cover is adjusted to 2 mm. The air in the gap causes the surface of the liquid metal to oxidize. This thin oxide layer gives rise to no-slip conditions for the velocity components parallel to the surface. However, the oxide layer does not prevent surface deformation.

To heat the upper surface we use a standard electrical heater which basically consists of a cylinder made of stainless steel with a Ni–Cr heating wire in its interior. The diameter of the heater is $2 \times r_{\mathrm{H}} = 12$ mm. The heater produces a maximum power

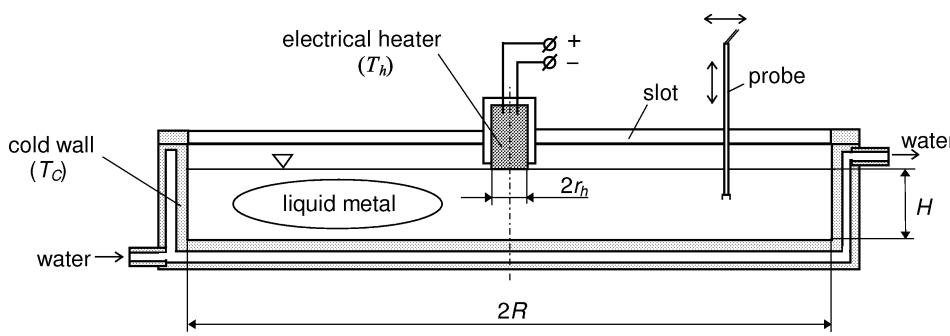

Fig. 1. Sketch of the experimental set-up. The aspect ratio of the cell is $R/H = 4.125$.

Table 1
Material properties of eutectic GaInSn at $T = 20\,^{\circ}\mathrm{C}$

ρ kg/m^3	ν m^2/s	λ W/(mK)	α K^{-1}	c_p J (kgK)	σ (Ohm·m)$^{-1}$	Pr (100 °C)
6360	3.4×10^{-7}	39	1.32×10^{-4}	366	3.3×10^{6}	2.03×10^{-2}

of $Q = 450$ W. With this actual setup we achieve heat flux densities $q = Q/(\pi r_H^2)$ of up to $q = 4.0 \times 10^6$ W/m^2. During the experiments, the heater is submerged 0.5 mm deep into the liquid metal. A thin layer of tin covers the bottom of the heater. Thus, the dissolving tin enables a durable heat contact between the heater and the melt. The heater is fixed to the cover plate in the centerline with a position precision of 0.1 mm. To quantify buoyancy forces induced by the heater we introduce a Rayleigh number defined by

$$Ra = \frac{\alpha g (q/\lambda) H^4}{\nu\kappa}. \tag{1}$$

Here, the material properties of the liquid metal are the thermal expansion coefficient α, heat conductivity λ, the kinematic viscosity ν, and the thermal diffusivity κ, while g denotes the acceleration of gravity. As the characteristic length scale of the present problem we choose the liquid layer height H. This choice takes into account that in large-aspect ratio containers the expected flow field consists of convection rolls of typical dimension H. In the experiments we vary the Rayleigh number within the range $1.0 \times 10^5 \leqslant Ra \leqslant 3.6 \times 10^6$.

The homogenous vertical magnetic field is generated by a direct current solenoid within which the container was arranged. The solenoid used produces magnetic inductions of up to $B_0 = 0.1$ T. The effects of the magnetic field are characterized by the Hartmann number defined by

$$Ha = B_0 H \left(\frac{\sigma}{\rho_0 \nu} \right)^{1/2}. \tag{2}$$

Here, σ denotes the electrical conductivity of the liquid metal and ρ_0 its reference density. During the experiments we vary the Hartmann number within the range $0 \leqslant Ha \leqslant 80$.

2.2. Measurement techniques

We measure cross-sectional time-averaged temperature distributions within the melt using a copper-constantan thermocouple with a sensitivity of 40 μV/K. The thermocouple is mounted in a stainless steel tube with a diameter of 0.5 mm. The tube serves as both electrical insulator and corrosion prevention. To move the thermocouple in radial and vertical direction we use computer-controlled positioning system especially designed for this task. The temperature T_H of the liquid/heater interface is measured by a similar thermocouple which touches the center of the heater bottom. We control the temperature T_C of the cooled side by another thermocouple which is attached to the inner wall of the container. With the data obtained we introduce the temperature difference $\Delta T = T_H - T_C$ and define the Nusselt number Nu as

$$Nu = \frac{\Delta T_0}{\Delta T}. \tag{3}$$

Here, ΔT_0 denotes the temperature difference in the motionless state. The particular value ($\Delta T_0 = 0.271$ in dimensionless units) is obtained numerically, cf. Section 3 and Fig. 4. When convective motion sets in, we have $\Delta T < \Delta T_0$. Thus, the Nusselt number characterizes the convective heat losses. Our overall goal shall be to measure the Nusselt number as a function of the Rayleigh number and the Hartmann number, i.e. to determine the functional relation

$$Nu = Nu(Ra, Ha). \tag{4}$$

Velocity measurements in liquid metals are generally difficult to perform because of the opacity and aggressiveness of the melt at high temperatures. We use an electrical potential probe (Knebel and Krebs [27]) to measure both the radial and azimuthal velocity components. Fig. 2 shows a sketch of the probe. It consists of a cylindrical permanent magnet with a diameter of 4 mm and a height of 5 mm, and four electrically insulated copper electrodes with a diameter of 0.25 mm. The magnet generates a static magnetic field in upward direction. Each pair of opposite electrodes measures the electric potential difference which is induced by the interaction of the liquid metal flow with the field of the permanent magnet. The respective velocity component is directly proportional to the measured potential difference. The sensitivity of the probe used is 1.2 μV/(cm/s). Moreover, four thermocouples record the actual temperature difference between corresponding electrodes to account for thermoelectric effects. These effects seemingly produce a velocity signal which we can calculate and take off. To move the probe within the liquid metal we use the same positioning system as for the temperature measurements. A drawback of the velocity measurement technique used is that it fails in the presence of a strong external magnetic field.

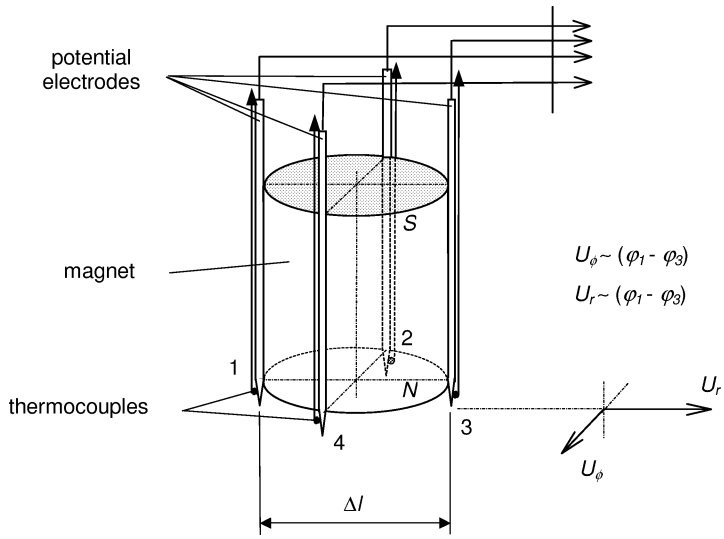

Fig. 2. Sketch of the electrical potential probe used for velocity measurement.

3. Numerical simulations

3.1. Governing equations

For the numerical simulations we consider the Boussinesq equations (cf. Platten and Legros [28]) in vorticity-streamfunction-temperature (ψ-ω-T) formulation for an axisymmetric geometry. The vorticity equation is equipped with an additional Lorentz force term to account for the influence of a constant vertical magnetic field $\mathbf{B} = B_0\mathbf{e_z}$. Applying the magnetohydrodynamic approximation (low magnetic Reynolds number, cf. Moreau [8]) to the present case, the Lorentz force $\mathbf{F_L}$ is given by

$$\mathbf{F_L} = -\frac{1}{\rho_0} B_0^2 \sigma u \mathbf{e_r}, \tag{5}$$

see the Appendix for details of this derivation. In dimensionless form we write the complete set of governing equations as follows:

$$\begin{aligned}&\left(\frac{\partial}{\partial t} + \frac{1}{r}\frac{\partial\psi}{\partial z}\frac{\partial}{\partial r} - \frac{1}{r}\frac{\partial\psi}{\partial r}\frac{\partial}{\partial z} - \frac{1}{r^2}\frac{\partial\psi}{\partial z}\right)\omega \\ &\quad = Pr\left(\frac{\partial^2}{\partial r^2} + \frac{1}{r}\frac{\partial}{\partial r} - \frac{1}{r^2} + \frac{\partial^2}{\partial z^2}\right)\omega - Pr\,Ra\frac{\partial}{\partial r}T - Pr\,Ha^2\frac{1}{r}\frac{\partial^2\psi}{\partial z^2},\end{aligned} \tag{6}$$

$$\left(\frac{\partial^2}{\partial r^2} - \frac{1}{r}\frac{\partial}{\partial r} + \frac{\partial^2}{\partial z^2}\right)\psi = r\omega, \tag{7}$$

$$\left(\frac{\partial}{\partial t} + \frac{1}{r}\frac{\partial\psi}{\partial z}\frac{\partial}{\partial r} - \frac{1}{r}\frac{\partial\psi}{\partial r}\frac{\partial}{\partial z}\right)T = \left(\frac{\partial^2}{\partial r^2} + \frac{1}{r}\frac{\partial}{\partial r} + \frac{\partial^2}{\partial z^2}\right)T. \tag{8}$$

We apply fixed temperature and fixed heat flux conditions at the walls and the upper surface, respectively. Moreover, the liquid metal obeys the no-slip condition at rigid boundaries. Furthermore, we use symmetry conditions along the line $r = 0$. These boundary conditions can be written as:

$$\psi = \frac{\partial\psi}{\partial z} = 0 \quad \text{at } z = 0 \text{ and } z = 1, \qquad \psi = \frac{\partial\psi}{\partial r} = 0 \quad \text{at } r = R/H, \tag{9a, b}$$

$$T = 0 \quad \text{at } z = 0 \text{ and } r = R/H, \qquad \frac{\partial}{\partial z}T = \begin{cases} 1, & 0 \leqslant r \leqslant r_H/H, \\ 0, & r_H/H < r \leqslant R/H, \end{cases} \tag{10a, b}$$

$$\psi = \omega = \frac{\partial T}{\partial r} = 0 \quad \text{at } r = 0. \tag{11}$$

Here, the vorticity ω and the streamfunction ψ are defined as:

$$\omega = \frac{\partial}{\partial z}u - \frac{\partial}{\partial r}w, \qquad u = \frac{1}{r}\frac{\partial}{\partial z}\psi, \qquad w = -\frac{1}{r}\frac{\partial}{\partial r}\psi. \tag{12a, b, c}$$

To derive the equations above we used the scales:

$$x, z \propto H, \qquad t \propto \frac{H^2}{\kappa}, \qquad T - T_0 \propto \frac{qH}{\lambda}, \qquad \omega \propto \frac{\kappa}{H^2}, \qquad \psi \propto \kappa H. \tag{13}$$

This scaling yields the dimensionless groups Rayleigh number *Ra* and Hartmann number *Ha* as already defined in Eq. (1) and Eq. (2), respectively. The diffusive properties of the liquid are characterized by the Prandtl number *Pr* given by

$$Pr = \frac{\nu}{\kappa}. \tag{14}$$

3.2. Numerical method

The governing equations shown above are numerically solved with a finite element method. We use linear triangles for spatial representation and the classical backward Euler scheme for time discretization. The nonlinear terms are treated explicitly. Starting from an appropriate initial condition, the governing equations are integrated in time until a (quasi) steady state emerges. During the integration the new time step is successively adjusted to satisfy the CFL stability criterion (cf. Press et al. [29]). At each time step the resulting sets of linear equations are solved iteratively using a Gauss–Seidel method with simultaneous over-relaxation, Chebyshev acceleration, and odd/even ordering (cf. Press et al. [29]).

During the simulations we fix parameters at $Pr = 0.02$, $R/H = 4.125$, and $r_H/H = 0.3$ to account for the experimental set-up. We vary the Rayleigh number and the Hartmann number within the ranges $0.25 \times 10^5 \leqslant Ra \leqslant 1.5 \times 10^6$ and $0 \leqslant Ha \leqslant 1.5 \times 10^2$. The calculations were carried out on a grid of 161×81 elements. It turned out that this grid size is sufficient since the Nusselt number typically changes less than 2% upon doubling the number of elements in each direction.

4. Results and discussion

4.1. The case $Ha = 0$

When the magnetic field is absent, i.e., $Ha = 0$, we can perform detailed measurements of the temperature and velocity fields using the electrical potential probe. Therefore, this case also allows a detailed comparison between experimental data and the results of numerical simulations.

4.1.1. Temperature field

We start the discussion by analyzing the obtained temperature fields. As an example, Fig. 3 shows measured isotherms for a heater power of $Q = 100$ W (Fig. 3(a)) and calculated isotherms at a corresponding Rayleigh number of $Ra = 0.825 \times 10^6$ (Fig. 3(b)). The graphs highlight the right half of the box in the range $0 \leqslant r \leqslant 40$ mm and $0 \leqslant z \leqslant 14$ mm within which almost the entire temperature drop occurs. We notice a good qualitative and quantitative agreement between the experimental data and the predictions of the numerical simulations. As expected, the hot spot is located directly below the center of the heater, i.e. at $r = 0$ and $z/H = 1$. In dimensional units, the measured temperature difference in the hot spot is $\Delta T_{HS} = 95\,^\circ$C while the predicted value is $\Delta T_{HS} = 92\,^\circ$C. The isotherms are considerably stretched in radial direction. This deviation from the hemispherically shaped conducting profile (cf. Fig. 10) indicates strong convective motion right underneath the surface from the hot center to the cold side wall. On the other hand, the isotherms are noticeably compressed below the heater. We conclude that this is due to intensive upward convection in this region.

In Fig. 4 the corresponding surface temperatures at $z/H = 1$ are drawn as a function of the radial coordinate r/H. For comparison the conducting profile is also given in Fig. 4 by the full line. We note that when convective heat transport is present, the temperature of the hot spot drops by about 23% as measured in experiment (cf. curve with circle symbols) and by about 26% as predicted by numerical simulation (cf. curve with square symbols), respectively. On the other hand, the radial convective heat transfer results in a corresponding increase of the surface temperature in the outer regions. In the vicinity of the heated zone the measured and predicted surface temperatures agree well as they deviate less than 4%. However, in the outer regions the measured surface temperature is considerably higher (for instance about 45% at $r/H = 2$) than the predicted ones. We attribute this discrepancy in the thermal fields to the actual differences in the velocity fields, as we shall see below. Moreover, at such high overall temperature differences ($\Delta T \approx 90$ K) non-Boussinesq effects, i.e. temperature-dependent fluid properties, may also contribute to such a deviation (cf. Platten and Legros [28]). Those effects are surely present in the experiment but were not accounted for in the simulation and in the evaluation of the Rayleigh number, cf. Eq. (11b).

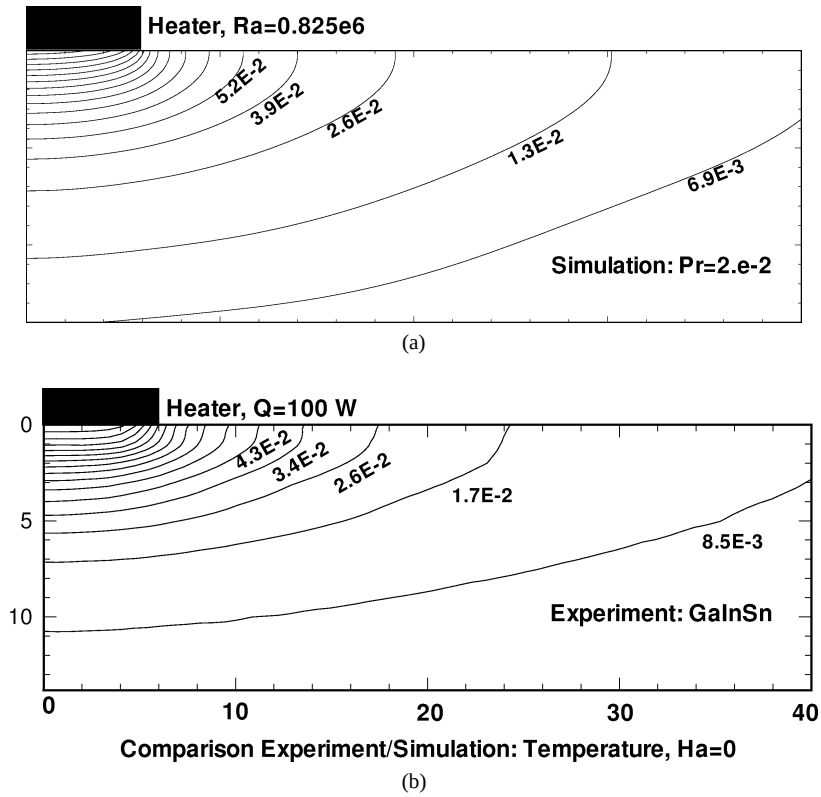

Fig. 3. Comparison experiment/simulation: temperature field for Hartmann number $Ha = 0$: (a) experimental results in GaInSn for heater power $Q = 100$ W; (b) numerical results for corresponding Prandtl number $Pr = 0.02$ and Rayleigh number $Ra = 0.825 \times 10^6$. The quantitative and qualitative agreement is good.

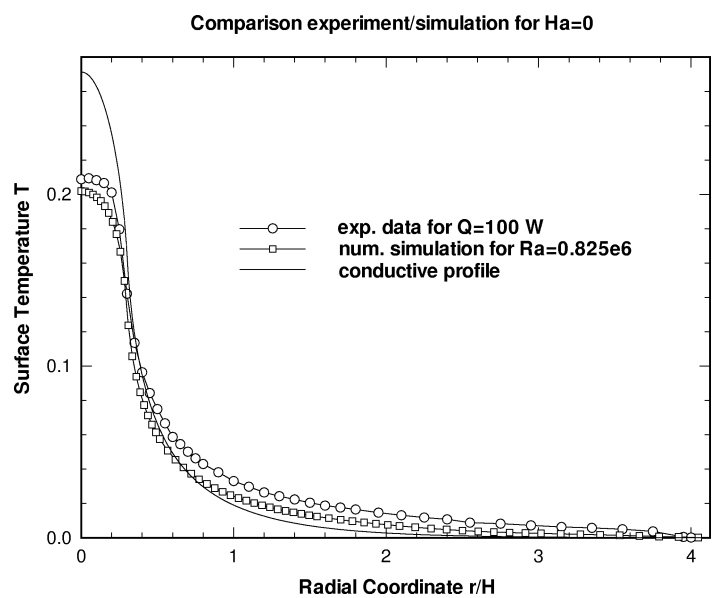

Fig. 4. Comparison experiment/simulation: surface temperature as function of radial coordinate r/H. Conducting profile (full line), experimental results for heater power $Q = 100$ W (circle symbols), numerical results for corresponding Rayleigh number $Ra = 0.825 \times 10^6$ (square symbols).

4.1.2. Velocity fields

Fig. 5 shows a comparison of radial velocity profiles $u(z)$ measured in experiment (curve marked by full diamond symbols) and predicted by simulation (curve marked by square symbols). Three different radial positions are taken, cf. positions 1, 2, and 3 shown in the inset of Fig. 6: $r/R = 0.25$ (i.e. $r/H = 1.03$) in Fig. 5(a), $r/R = 0.375$ ($r/H = 1.44$) in Fig. 5(b), and $r/R = 0.5$ ($r/H = 2.06$) in Fig. 5(c). Parameter values are the same as in Fig. 3. At position $r/R = 0.25$ we observe jet-like flow right beneath the upper surface. This jet is also reliably predicted by the numerical simulation. However, the measured jet is shifted closer to the surface and shows a slightly higher peak value. This feature corresponds to the fact that in the this region

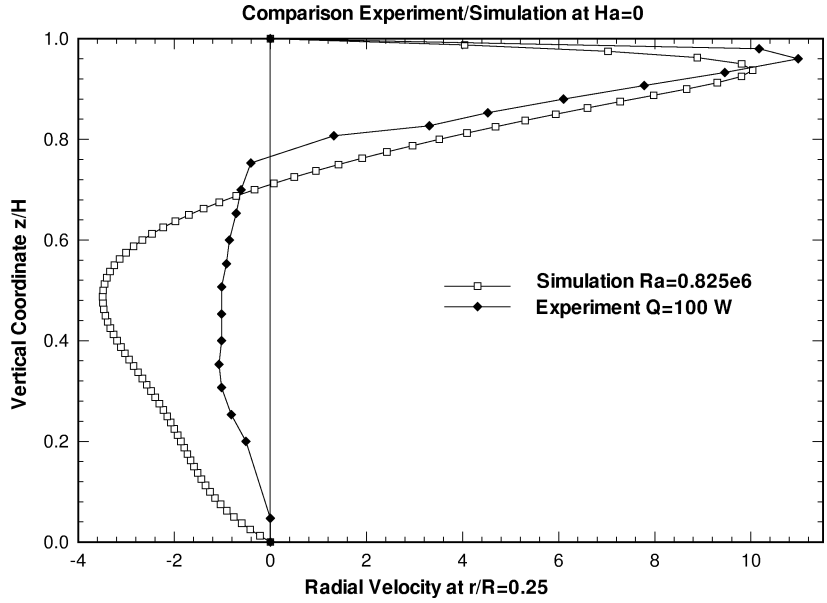

(a)

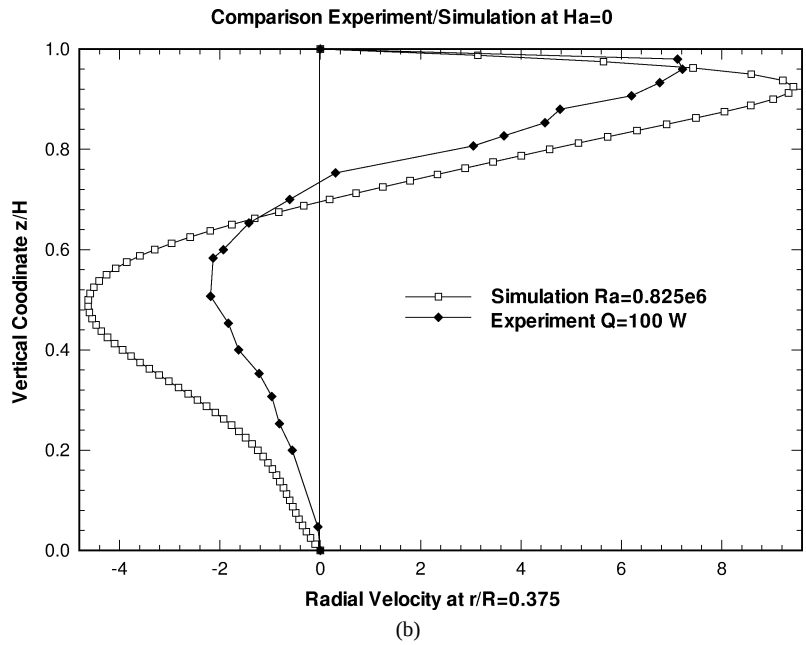

(b)

Fig. 5. Comparison experiment/simulation: Vertical profiles of radial velocity component. Experimental results for heater power $Q = 100$ W (full diamond symbols), numerical results for corresponding Rayleigh number $Ra = 0.825 \times 10^6$ (square symbols): (a) profiles at $r/R = 0.25$; (b) profiles at $r/R = 0.375$.

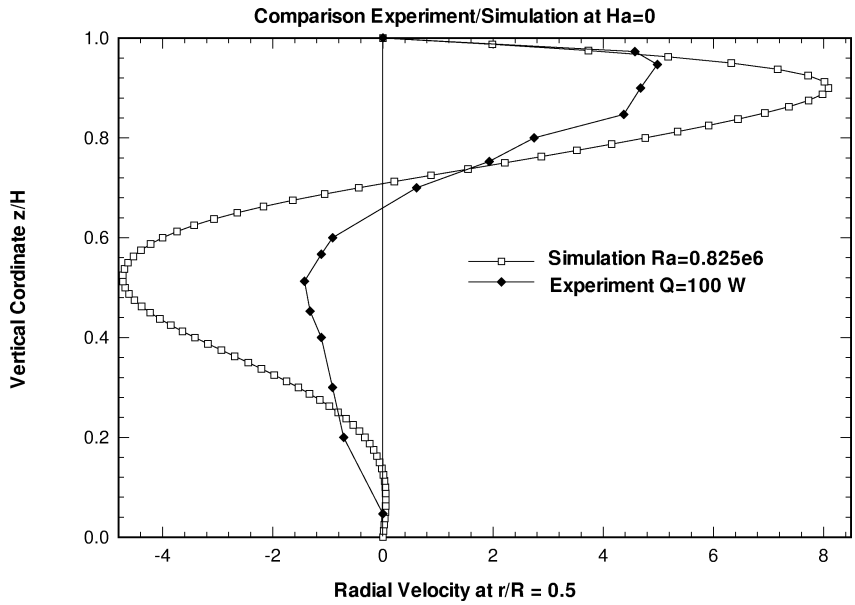

(c)

Fig. 5. (c) Profiles at $r/R = 0.5$.

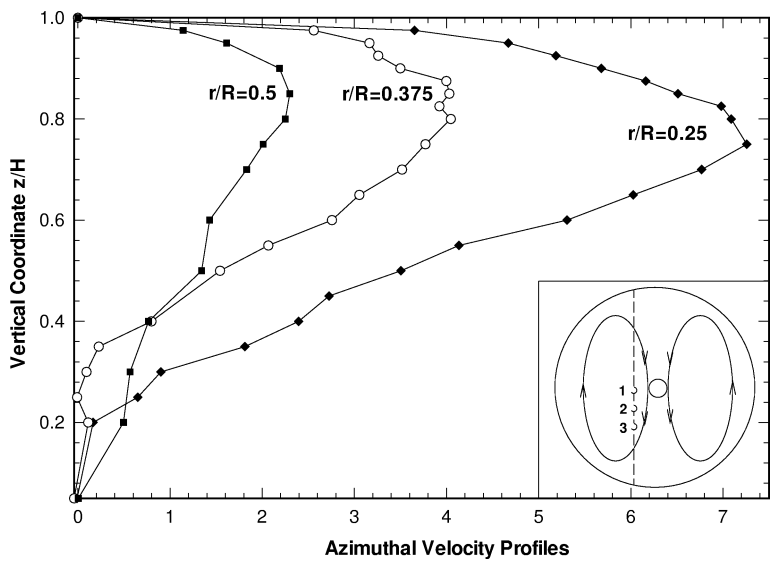

Fig. 6. Experimental results: Vertical profiles of azimuthal velocity component at radial positions $r/R = 0.25$ (full diamond symbols), $r/R = 0.375$ (circle symbols), and $r/R = 0.5$ (full square symbols). The inset shows a sketch of the dipolar structure of the flow field. Points 1, 2, and 3 mark positions at which the data was taken. The dashed vertical curve represents line of probe movement.

the measured temperature increase due to radial convective heat transport is higher than the predicted one, cf. Fig. 4. Physically, the jet is driven by a radial pressure gradient that is built up between the hot spot in the center and the cold lateral wall. This is also obvious from the vorticity equation (cf. Eq. (6)) where the radial temperature gradient acts as a production term. Upon increasing the distance from the heater the jet slows down and becomes thicker, see Figs. 5(b) and 5(c) for $r/R = 0.375$ and $r/R = 0.5$, respectively. This can be explained physically by the decrease of the driving radial temperature gradient and the action of molecular diffusion due to viscosity. It is noticeable that in these regions the predicted peak values are now higher than the measured ones. We ascribe this observation to three-dimensional effects which are present in the experiments but not taken into account in the simulations, see Fig. 6.

By continuity, below the jet a region adjoins that is characterized by reverse flow, see Fig. 5. This region occupies almost three quarters of the container height. However, the simulations predict a much more intensive reverse flow than that observed in experiment. We attribute this quantitative disagreement to the fact that in the simulations we assume two-dimensional axisymmetric flow, while our experiments show truly three-dimensional convective motion within the liquid metal. The 3D characteristics of the flow are depicted in Fig. 6. It shows azimuthal velocity profiles at the same radial positions as before, cf. positions 1, 2, and 3 in the inset of Fig. 6. It is remarkable that the peak values of the azimuthal component amount for up to 50% of those of the radial jet flow. As expected, the azimuthal convective motion also slows down in radial direction. The evaluation of our velocity measurements at different azimuthal and radial positions indicates that the global flow field shows dipolar characteristics. A sketch of the flow in a horizontal cross-section of the jet region is given in the inset of Fig. 6.

4.1.3. Heat transfer

A summary of our investigations in the absence of a magnetic field is shown in Fig. 7. Here we have plotted the Nusselt number as a function of the Rayleigh number. The experimental data span the range $1.0 \times 10^5 \leqslant Ra \leqslant 3.6 \times 10^6$, cf. curve with empty diamond symbols. On the other hand, the numerical simulations cover the range $0.25 \times 10^6 \leqslant Ra \leqslant 1.5 \times 10^6$, cf. curve with full diamond symbols. In this range the numerical results predict an interrelation according to

$$Nu^{(\mathrm{sim})} \propto Ra^{0.112}, \quad 0.25 \times 10^6 \leqslant Ra \leqslant 1.5 \times 10^6. \tag{15}$$

The corresponding experimental findings yield a dependence according to

$$Nu^{(\mathrm{exp})} \propto Ra^{0.160 \pm 0.010}, \quad 0.25 \times 10^6 \leqslant Ra \leqslant 1.5 \times 10^6. \tag{16}$$

We note that within this Rayleigh number range the predicted and measured Nusselt numbers are in good quantitative agreement as the particular values deviate not more than 5%. However, the qualitative agreement between experimental and numerical results is clearly worse as the exponents in the heat transfer relations equations (15) and (16) differ significantly by about 30%. We conclude that this qualitative discrepancy is directly related to the differences in the particular temperature and velocity fields. We have already pointed out above some effects (3D characteristics of the flow, non-Boussinesq behavior) that may explain this difference. Additionally, the used numerical method (see Section 3.2) may tend to underestimate the convective heat transfer.

In the range of higher Rayleigh numbers, i.e., $2.7 \times 10^6 \leqslant Ra \leqslant 3.6 \times 10^6$, the experimental data indicate a heat transfer relation according to

$$Nu^{(\mathrm{exp})} \propto Ra^{0.191 \pm 0.011}, \quad 2.7 \times 10^6 \leqslant Ra \leqslant 3.6 \times 10^6, \tag{17}$$

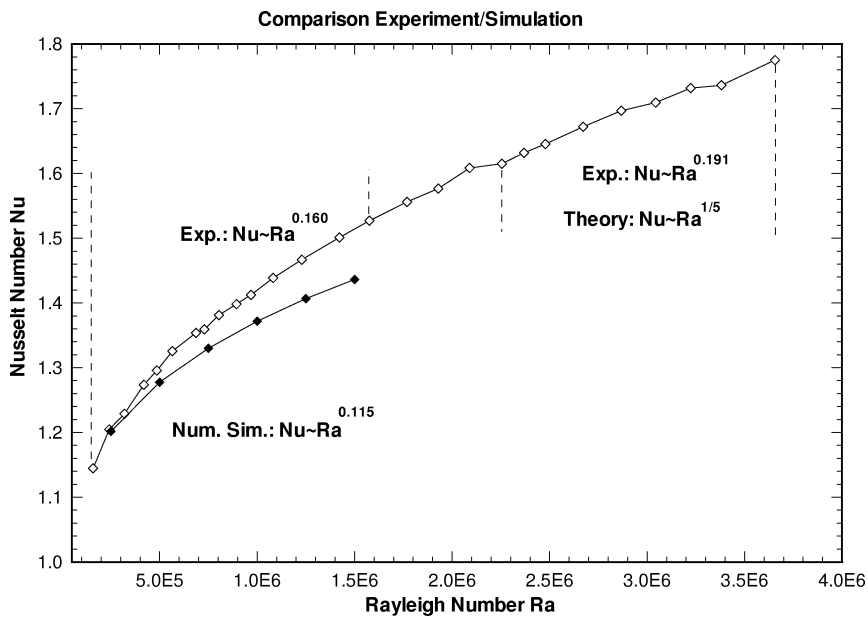

Fig. 7. Comparison experiment/simulation: Nusselt number as function of Rayleigh number for Hartmann number $Ha = 0$. Experimental results (diamond symbols) and numerical results (full diamond symbols). Vertical dashed lines mark range of Rayleigh numbers within which scaling exponents are calculated.

cf. Fig. 7. It is instructive to compare this experimental finding with predictions of a scaling analysis. Müller and Ehrhard [30] have recently presented such an analysis for the case of laminar convective flow in a low-Prandtl number fluid underneath a heated plate. Following the ideas of Schulenberg [31] these authors assume that the flow shows boundary layer characteristics and use matched asymptotics to solve for the velocity and temperature field within the boundary layer and the core. Eventually they find the scaling relations

$$Nu^{(\mathrm{th})} \propto Ra^{1/5} \quad \text{(plate at fixed temperature)}, \tag{18a}$$

$$Nu^{(\mathrm{th})} \propto Ra^{1/6} \quad \text{(plate at fixed heat flux)}. \tag{18b}$$

The excellent agreement between the theoretical prediction, Eq. (18), and the experimental finding equation (17) may validate both the assumptions made in the analysis and the quality of our measurements.

4.2. The case $Ha \neq 0$

We now examine the case when the static vertical magnetic field is present, i.e., $Ha \neq 0$. Due to the strong external field in this case it is no longer possible to use the electrical potential probe for velocity measurements. Therefore, in the experiments we focus on recording the Nusselt number. However, details of the convective flow are analyzed employing numerical simulations.

4.2.1. Temperature field

We first study the influence of the magnetic field on the thermal field. As a result of numerical simulations Fig. 8 shows the temperature of the hot spot as a function of the Hartmann number. In this example the Rayleigh number was fixed at $Ra = 1.5 \times 10^6$. In Fig. 8 the upper horizontal line represents the hot spot temperature for the motionless state of heat conduction. Moreover, Fig. 8 also shows the corresponding temperature fields for the two extreme cases $Ha = 0$, and $Ha = 150$, and the case of heat conduction, see the insets. We recognize that an applied vertical magnetic field indeed shows the desirable effect of reducing the convective heat losses. When a strong magnetic field is present ($Ha = 150$), the numerical simulation predicts an increase of the hot spot temperature of about 30% compared to the case $Ha = 0$, cf. curve with square symbols in Fig. 8. The contours of the isotherms make it obvious that the temperature field tends to take on the hemispherical shape of the conductive state under the action of a strong magnetic field, cf. insets in Fig. 8. This clearly indicates that for strong magnetic fields convective heat transfer is strongly suppressed. However, a relatively weak magnetic field of $Ha = 10$ does not contribute to a decrease of the convective heat losses, cf. Fig. 8. To the contrary, the temperature in the hot spot even slightly decreases in this case. This phenomenon can be explained physically by the fact that the presence of a weak magnetic field tends to

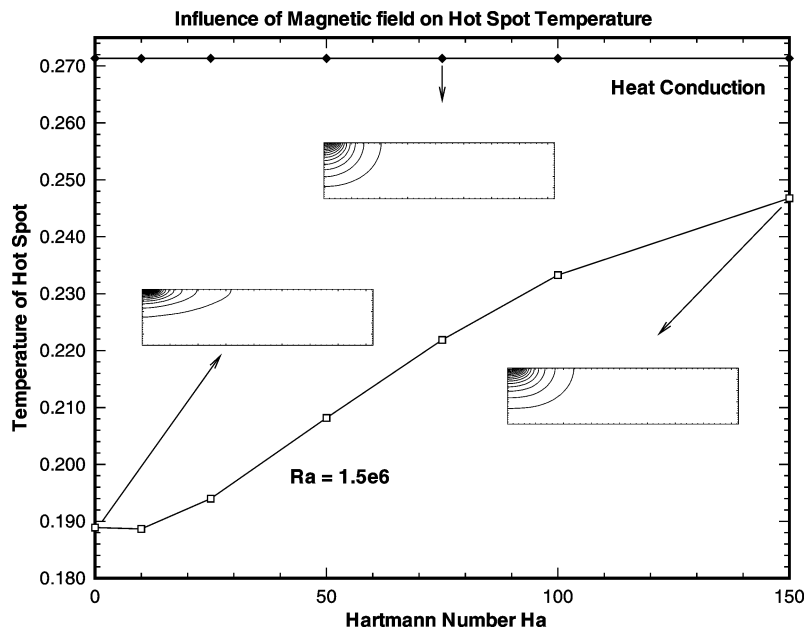

Fig. 8. Numerical results: Temperature in hot spot as function of Hartmann number for Rayleigh number $Ra = 1.5 \times 10^6$. The upper horizontal line represents state of heat conduction. Insets show corresponding temperature fields.

stabilize the radial jet flow underneath the surface, cf. also Fig. 9 below. More precisely, the jet does not separate anymore along the upper surface as for the case $Ha = 0$ but extends to the cold side wall. The stabilizing effect of a weak magnetic field counterbalances the weak dampening effect. The enhancement of convective heat transfer by weak magnetic fields was also found in the numerical studies of Li et al. [26], and Tagawa and Ozoe [24].

4.2.2. Velocity fields

The main effect of a strong vertical magnetic field, namely dampening of convective motion, becomes more evident when analyzing the velocity and vorticity fields. Fig. 9 shows a plot of streamlines obtained by numerical simulation. The lower graph refers to the case $Ha = 0$ while the upper graph highlights the case when a strong magnetic field of $Ha = 150$ is present. Again, the Rayleigh number was fixed at $Ra = 1.5 \times 10^6$. For $Ha = 0$ the global flow field consists of one convection roll of strong intensity with jet-like radial flow underneath the upper surface and reverse flow in the bottom region. The liquid rises below the heated zone and falls down the cold wall. Moreover, there are also two small-scale convection rolls of much weaker intensity at radial position $r/H = 2$ and $r/H = 3.2$, respectively. The small-scale secondary rolls result from the thickening of the radial jet along the upper surface, cf. Fig. 5, which eventually leads to its separation. Here the primary flow branches off into the bulk and separates again at the bottom. In contrast, when the magnetic field is present the small-scale secondary structures disappear. This indicates that the radial jet is stabilized because separation at top and bottom boundary is suppressed. The intensity of convection strongly decreases and the center of the global convection roll moves towards the heated zone. Fig. 10 shows the corresponding isolines of vorticity. In the case $Ha = 0$ the field is characterized by intensive vorticity production along the upper surface and the generation of small-scale secondary vortices in the interior of the liquid metal due to jet separation. Again, when the magnetic field is present the small-scale structures vanish. The net production of vorticity, restricted to a thin layer in the vicinity of the upper surface, is clearly diminished. The magnetic damping of jets and vortices has been studied intensively by Davidson [11,16]. The phenomena described above may be explained physically with the help of the governing equations, cf. equations (6) and (7). When the magnetic field is present, the production term of vorticity ($\propto Ra(\partial T/\partial r)$) competes with a sink term ($\propto \frac{1}{r}Ha^2(\partial^2\psi/\partial z^2)$) that preferentially acts near the centerline and in regions with a high velocity gradient ($\partial u/\partial z$). Hence, the magnetic field mainly suppresses the jet-like flow which was identified as the basic source of the high convective heat losses. This conclusion is also supported by Fig. 11 which shows profiles of the radial velocity component at position $r/R = 0.5$ as a function of the Hartmann number. Upon increasing the strength of the magnetic field from $Ha = 0$ to $Ha = 150$,

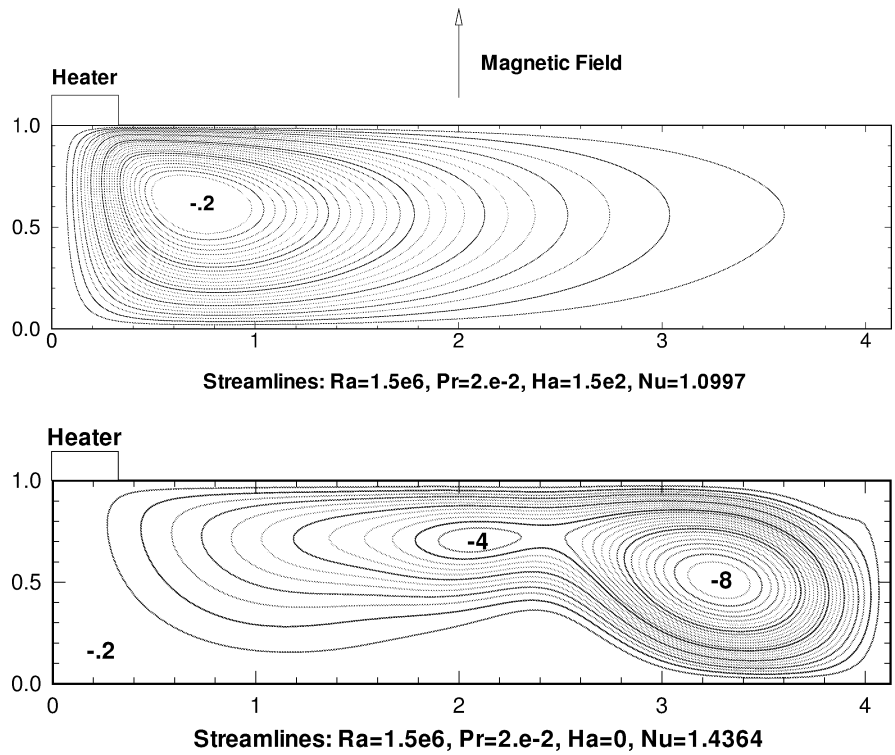

Fig. 9. Numerical results: Plot of streamlines for Rayleigh number $Ra = 1.5 \times 10^6$ and Hartmann numbers $Ha = 0$ (lower graph) and $Ha = 150$ (upper graph).

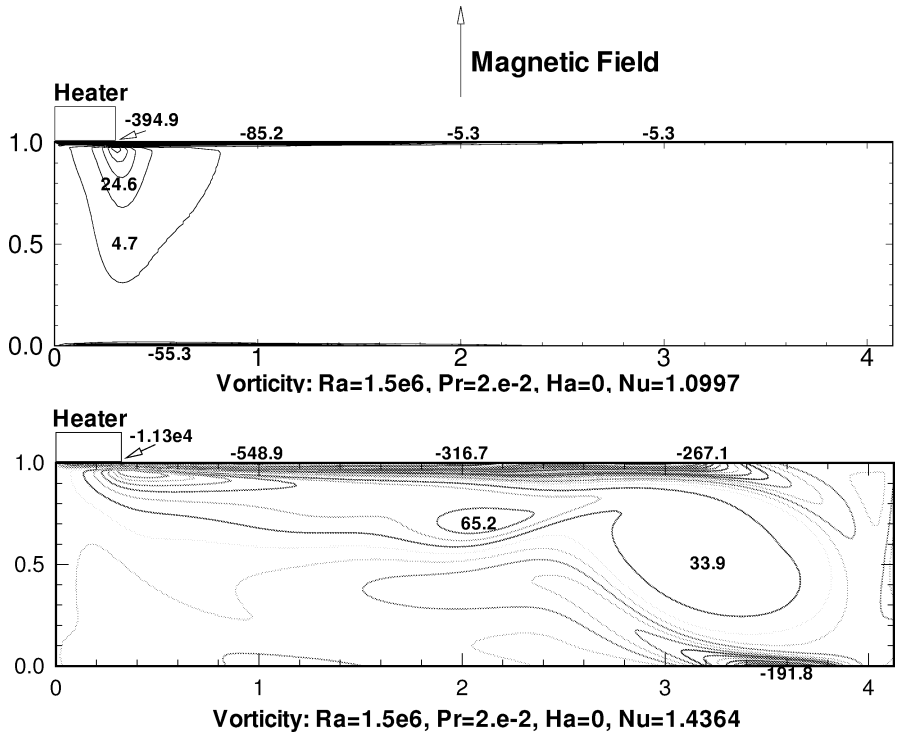

Fig. 10. Numerical results: Plot of vorticity field for Rayleigh number $Ra = 1.5 \times 10^6$ and Hartmann numbers $Ha = 0$ (lower graph) and $Ha = 150$ (upper graph).

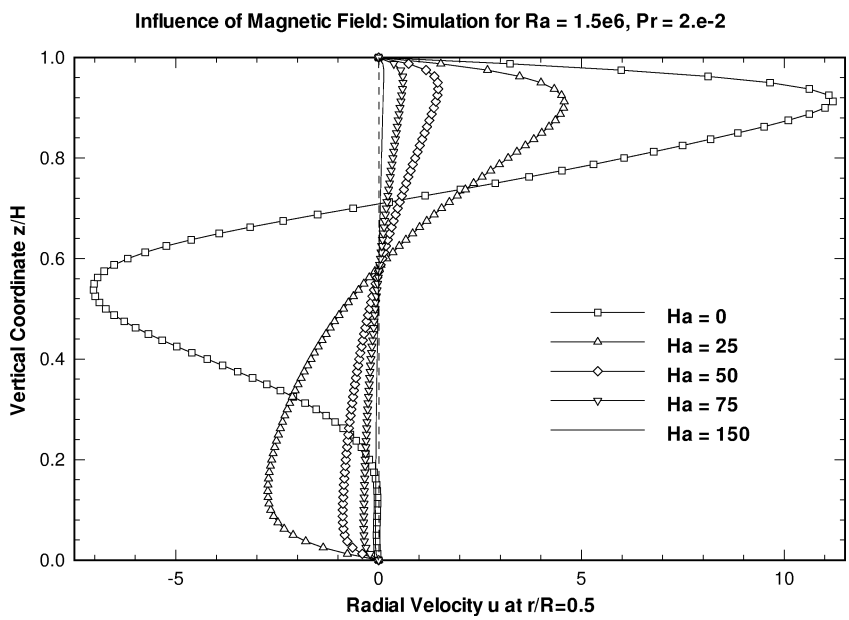

Fig. 11. Numerical results: Vertical profiles of radial velocity component at position $r/R = 0.5$ for Rayleigh number $Ra = 1.5 \times 10^6$ and Hartmann numbers $Ha = 0$ (square symbols), $Ha = 25$ (triangle symbols), $Ha = 50$ (diamond symbols), $Ha = 75$ (gradient symbols), and $Ha = 150$ (full line). The vertical dashed line represents $u = 0$.

the peak value of the jet is reduced by about two orders of magnitude. By continuity, the intensity of the reverse flow also decreases drastically. The dampening effect on radial convective motion results from the radial Lorentz force ($\mathbf{F_L} \propto -u\mathbf{e_r}$, cf. equation (5)) that is induced by the magnetic field.

It is interesting to investigate the characteristics of the flow for higher Hartmann numbers. In this case our numerical results can be compared with predictions of a scaling analysis valid for the asymptotic limit $Ha \gg 1$, cf., e.g., Hjellming and Walker [22], and Alboussiere et al. [32]. The analysis shows that near the upper surface a so-called Hartmann layer forms within which viscous and magnetic forces balance. The thickness δ_H of this layer and the characteristic dimensionless velocity u in the layer turn out to scale as follows:

$$\delta_H/H \propto Ha^{-1}, \qquad u \propto Ha^{-2}. \tag{19a, b}$$

We perform detailed numerical simulations for the present problem in the range $320 \leqslant Ha \leqslant 330$ for a Rayleigh number of $Ra = 1.5 \times 10^6$. In this range we find the scaling relation according to

$$u \propto Ha^{-2.0534}. \tag{20}$$

The excellent agreement between the predicted and calculated scaling exponents may validate our numerical approach.

4.2.3. Heat transfer

We finally discuss the influence of the magnetic field on the convective heat transfer within the melt. Fig. 12 presents the Nusselt number as a function of the Hartmann number for various Rayleigh numbers. The experimental results are given in Fig. 12(a) while the findings of the numerical simulations are shown in Fig. 12(b). For comparison, in Fig. 12(a) the numerical results for the case $Ra = 1.25 \times 10^6$ are also given by the full circle symbols. Both graphs clearly demonstrate that a strong magnetic field applied in vertical direction significantly reduces the Nusselt number due to the suppression of convective motion. However, a detailed quantitative comparison between the data and the simulations reveals that the calculations predict lower Nusselt numbers than observed in experiment. For the case $Ha = 0$ we have already listed some effects that contribute to such a difference. These conclusions should also apply for the case when the magnetic field is present. This difference becomes less pronounced for higher Hartmann numbers, cf. the empty and the full circle symbols in Fig. 12(a). This effect may be explained by the fact that the three-dimensional characteristics of the flow become less pronounced in the presence of a strong magnetic field. However, the overall qualitative agreement we achieve is remarkable. For instance, upon increasing the Hartmann number from $Ha = 0$ to $Ha = 80$ the experimental data indicate a reduction of the Nusselt number of about 17%, cf. the curve for $Ra = 1.2375 \times 10^6$ in Fig. 12(a). On the other hand, the numerical results predict a decrease of about 15% within the same Hartmann number range, cf. curve for $Ra = 1.25 \times 10^6$ in Fig. 12(b) and full circle symbols in Fig. 12(a). As indicated by the numerical findings the reduction of the Nusselt number becomes less effective for stronger magnetic fields ($Ha > 80$), see Fig. 12(b). This was expected, since in the limit $Ha \to \infty$ the Nusselt number asymptotically approaches the value $Nu \to 1$. This tendency is also observed in the experiments at smaller Rayleigh numbers, cf. Fig. 12(a). Furthermore, the numerical results yield that relatively weak magnetic fields ($Ha = 10$) do not contribute to a reduction of the convective heat losses, see Fig. 12(b) and cf. Section 3.2.1. This phenomenon is especially pronounced at high Rayleigh numbers. In the experiments we also observe the decrease of the Nusselt number at low Hartmann numbers, cf. curve for $Ra = 1.2375 \times 10^6$ in Fig. 12(a). These results are consistent with findings of Li et al. [26] and Tagawa and Ozoe [24].

5. Summary

We have investigated both experimentally and numerically the influence of a static vertical magnetic field on the buoyancy-driven convective heat transfer in a liquid metal heated locally at its upper surface. The arrangement studied serves as a physical model for the industrial process of electron beam evaporation of liquid metals. In the experiments we use eutectic GaInSn as the working fluid. The actual set-up allows measurement of both temperature and velocity using an electric potential probe. The numerical simulations are based on the Boussinesq equations in a two-dimensional axisymmetric geometry. When the magnetic field is absent ($Ha = 0$) the measurements yield a heat transfer correlation according to the law $Nu \propto Ra^{0.191\pm0.011}$ within the range $2.7 \times 10^6 \leqslant Ra \leqslant 3.6 \times 10^6$. The particular exponent is in good agreement with the prediction $Nu \propto Ra^{0.2}$ of a scaling analysis for natural convection of a low-Prandtl number fluid underneath a heated plate. The results of the numerical simulations performed within the range $0.25 \times 10^6 \leqslant Ra \leqslant 1.5 \times 10^6$ indicate a much lower exponent of 0.112. We attribute this deviation to the fact that in this range the asymptotic regime assumed in the analysis has not yet developed. When a magnetic field magnetic fields of moderate strength ($Ha = 150$) is applied, the Nusselt number decreases by about 20% compared to the case $Ha = 0$. This decrease is due to the dampening effect of a static magnetic field. We achieve a good qualitative agreement between the experimental data and the predictions of the numerical simulations. We conclude that quantitative differences result from three-dimensional flow characteristics and non-Boussinesq effects, all of which are present in the experiment but not accounted for in the simulations. Our numerical results agree well with predictions of a scaling analysis for the limiting case $Ha \to \infty$.

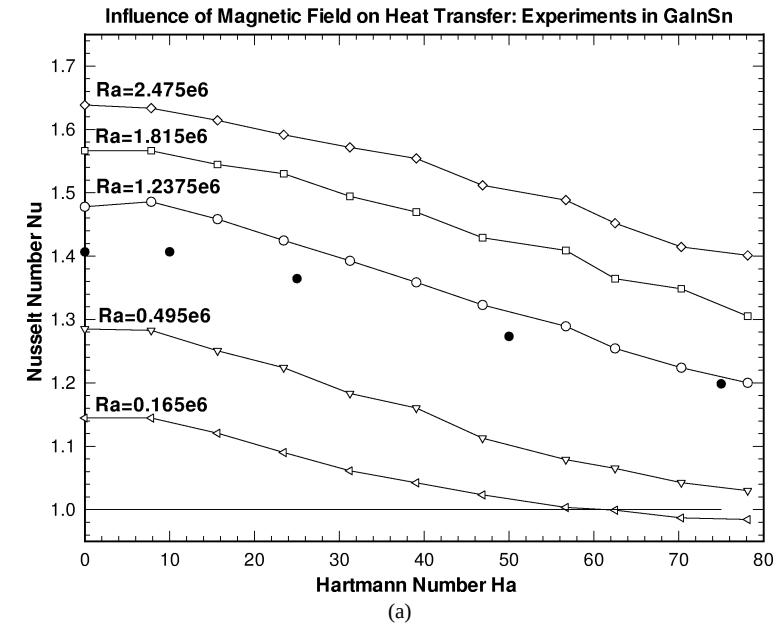

(a)

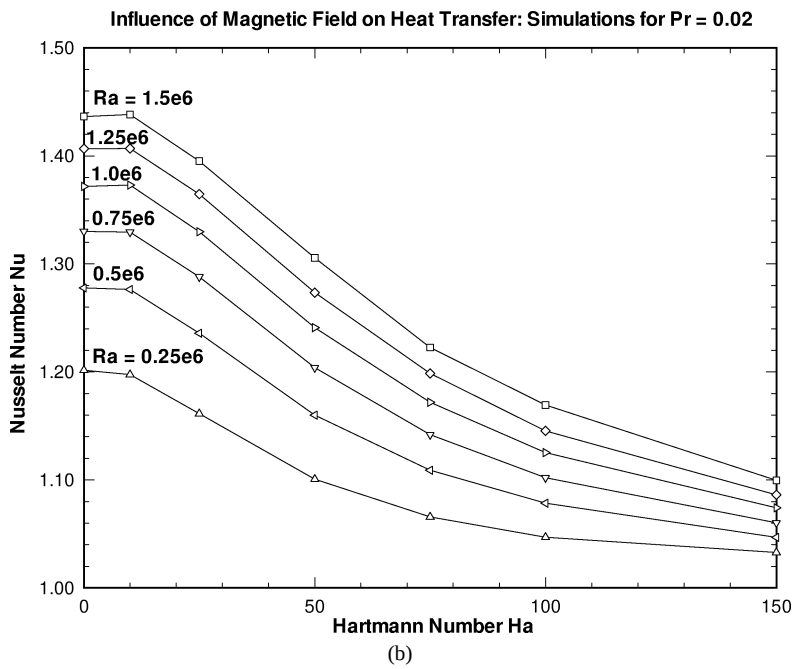

(b)

Fig. 12. Comparison experiment/simulation: Nusselt numbers as function of Hartmann numbers for various Rayleigh numbers: (a) experimental results for $Ra = 2.475 \times 10^6$ (diamond symbols), $Ra = 1.815 \times 10^6$ (square symbols), $Ra = 1.2375 \times 10^6$ (circle symbols), $Ra = 0.495 \times 10^6$ (gradient symbols), and $Ra = 0.165 \times 10^6$ (left pointed triangles). The full circle symbols mark individual data points of numerical results for $Ra = 1.25 \times 10^6$; (b) Numerical results for $Ra = 1.5 \times 10^6$ (square symbols), $Ra = 1.25 \times 10^6$ (diamond symbols), $Ra = 1.0 \times 10^6$ (right pointed triangles), $Ra = 0.75 \times 10^6$ (gradient symbols), $Ra = 0.5 \times 10^6$ (left pointed triangles), and $Ra = 0.25 \times 10^6$ (triangle symbols).

Acknowledgements

This work was sponsored by the Deutsche Forschungsgemeinschaft under grant Th-C3.1. The authors would like to acknowledge helpful comments from R. Schaller and P.A. Davidson.

Appendix A. Derivation of the Lorentz force in magnetohydrodynamic approximation (cf. equation (5))

The Lorentz force $\mathbf{F_L}$ is defined as follows, cf. Moreau [8]:

$$\mathbf{F_L} = \frac{1}{\rho}\mathbf{j} \times \mathbf{B}, \tag{A.1}$$

where $\mathbf{j}$ is the (induced) current density and $\mathbf{B}$ the (applied plus induced) magnetic field. The current density obeys Ampere's law while the dynamics of the magnetic field is governed by the induction equation. In dimensionless form these equations become:

$$\mathbf{j} = \nabla \times \mathbf{B}, \tag{A.2}$$

$$\frac{\partial}{\partial t}\mathbf{B} = \nabla \times (\mathbf{v} \times \mathbf{B}) + \frac{1}{Re_{\mathrm{m}}}\nabla^2\mathbf{B}, \tag{A.3}$$

where $Re_m = \sigma\mu UL$ is the magnetic Reynolds number. We now evaluate Eqs. (A1), (A2) in the magnetohydrodynamic approximation $Re_{\mathrm{m}} \ll 1$ and introduce the ansatz

$$\mathbf{B} = B_0\mathbf{e_z} + Re_{\mathrm{m}}\mathbf{b}, \tag{A.4}$$

where B_0 is the applied and $\mathbf{b}$ the induced magnetic field. We insert ansatz (A4) into Eqs. (A2), (A3). After some straightforward vector algebra, to the order $\mathrm{O}(Re_{\mathrm{m}})$ we obtain $(\partial/\partial t \equiv 0)$

$$\mathbf{j} = \nabla \times \mathbf{b}, \tag{A.5}$$

$$\mathbf{b} = -\left(\nabla^{\mathbf{2}}\right)^{-1}\frac{\partial}{\partial z}\mathbf{v}, \tag{A.6}$$

where $(\nabla^2)^{-1}$ formally denotes the inverse Laplacian. Finally, we insert ansatz (A4) into the dimensionless form of equation (A1) and use Eqs. (A5) and (A6). For the present case of two-dimensional axisymmetric flow we obtain:

$$\mathbf{F_L} \propto -u\mathbf{e_r}. \tag{A.7}$$

References

[1] S. Schiller, U. Heisig, S. Panzer, Electron Beam Technology, Wiley, New York, 1982.
[2] S.H. Davis, Thermocapillary instabilities, Annu. Rev. Fluid Mech. 19 (1987) 403–435.
[3] E.D. Siggia, High Rayleigh number convection, Annu. Rev. Fluid Mech. 26 (1994) 137–168.
[4] A. Pumir, L. Blumenfeld, Heat transport in a liquid layer locally heated on its free surface, Phys. Rev. E 54 (1996) 4528–4531.
[5] E. Favre, L. Blumenfeld, F. Daviaud, Instabilities of a liquid layer locally heated on its upper surface, Phys. Fluids 9 (1997) 1473–75.
[6] Ch. Karcher, R. Schaller, Th. Boeck, Ch. Metzner, A. Thess, Turbulent heat transfer in liquid iron during electron beam evaporation, Int. J. Heat Mass Tran. 43 (2000) 1759–66.
[7] Ch. Karcher, R. Schaller, A. Thess, Convective heat transfer during electron beam evaporation of liquid metals, in: El-Kaddah N. et al. (Eds.), Fluid Flow Phenomena in Metals Processing, TMS Publication, Warrendale, PE, 1999.
[8] R. Moreau, Magnetohydrodynamics, Kluwer, Dordrecht, 1990.
[9] Ph. Marty, L. Martin-Witkowski, Control of thermal Marangoni convection in electron beam technology, Int. J. Thermal Sci. 39 (2000) 285–294.
[10] Ch. Karcher, U. Lüdtke, D. Schulze, A. Thess, Electromagnetic control of melt-flow in electron beam evaporation Part 2: numerical simulations, in: Proc. 3rd Int. Symposium on Electromagnetic Processing of Materials, Nagoya, 2000, pp. 473–478.
[11] P.A. Davidson, Magnetohydrodynamics in materials processing, Annu. Rev. Fluid Mech. 31 (1999) 273–300.
[12] S. Chandrasekhar, Hydrodynamic and Hydromagnetic Stability, Oxford University Press, New York, 1961.
[13] A. Boyarevich, L. Gorbunov, Effect of magnetic fields of different orientation on thermogravitational convection in an electrically conducting fluid with horizontal heat flow, Magnetohydrodynamics 24 (1988) 17–24.
[14] S. Fauve, C. Laroche, A. Libchaber, Effect of a horizontal magnetic field on convective instabilities in mercury, J. Phys. Lett. 42 (1981) 455–457.
[15] H.K. Moffat, On the suppression of turbulence by a uniform magnetic field, J. Fluid Mech. 28 (1967) 571–592.
[16] P.A. Davidson, Magnetic damping of jets and vortices, J. Fluid Mech. 299 (1996) 153–186.
[17] P. Rivat, J. Etay, M. Garnier, Stabilization of a surface wave by a magnetic field, Eur. J. Mech B/Fluids 10 (1991) 135–148.
[18] P.A. Davidson, R.I. Lindsay, Stability of interfacial waves in aluminum reduction cells, J. Fluid Mech. 362 (1998) 273–295.
[19] R.W. Series, D.T.J. Hurle, The use of magnetic fields in semiconductor crystal growth, J. Cryst. Growth 113 (1991) 305–328.
[20] D.D. Papaliliou, P.S. Lykoudis, Magneto-fluid-mechanics free convection turbulent flow, Int. J. Heat Mass Tran. 17 (1974) 1181–1189.
[21] M. Seki, H. Kawamura, K. Sanokawa, Natural convection of mercury in a magnetic field parallel to gravity, J. Heat Trans.-T ASME 101 (1979) 227–232.

[22] L.N. Hjellming, J.S. Walker, Melt motion in a Czochalski crystal puller with an axial magnetic field: Motion due to buoyancy and thermocapillarity, J. Fluid Mech. 182 (1987) 335–368.
[23] K. Okado, H. Ozoe, Experimental heat transfer rates of natural convection of molten gallium suppressed under an external magnetic field in either X, Y, or Z direction, J. Heat Tran. 114 (1992) 107–114.
[24] T. Tagawa, H. Ozoe, Enhancement of heat transfer rate by application of a static magnetic field during natural convection of liquid metal in a cube, J. Heat Trans-T. ASME 119 (1997) 265–271.
[25] A. Juel, T. Mullin, H. Ben Hadid, D. Henry, Magnetohydrodynamic convection in molten gallium, J. Fluid Mech. 378 (1999) 97–118.
[26] B.Q. Li, X. Lu, H.C. De Groh, Finite element modeling of magnetically damped convection in conducting melts, in: El-Kaddah N. et al. (Eds.), Fluid Flow Phenomena in Metals Processing, TMS Publication, Warrendale, PE, 1999.
[27] J.U. Knebel, L. Krebs, Calibration of a miniature permanent magnet flow meter probe and its application to velocity measurements in liquid sodium, Exp. Therm. Fluid Sci. 8 (1994) 135–148.
[28] J. Platten, J. Legros, Convection in Liquids, Springer, New York, 1984.
[29] W.H. Press, S.A. Teukolsky, W.T. Vetterling, B.B. Flannery, Numerical Recipes in Fortran 77, Cambridge University Press, New York, 1992.
[30] U. Müller, P. Ehrhard, Freie Konvektion und Wärmeübertragung, Verlag C.F. Müller, Heidelberg, 1999.
[31] Th. Schulenberg, Natural convection heat transfer to liquid metals below downward facing horizontal surfaces, Int. J. Heat Mass Trans. 27 (1984) 433–441.
[32] T. Alboussiere, J.P. Garandet, R. Moreau, Asymptotic analysis and symmetry in MHD convection, Phys. Fluids 8 (1996) 2215–2226.